

# Estimations of the magnetic field strength in the torus of AGN using near-infrared polarimetry.

E. Lopez-Rodriguez<sup>1,2\*</sup>, C. Packham<sup>1,2</sup>, S. Young<sup>3</sup>, M. Elitzur<sup>4</sup>, N. A. Levenson<sup>5</sup>,  
R. E. Mason<sup>6</sup>, C. Ramos Almeida<sup>7,8</sup>, A. Alonso-Herrero<sup>9†</sup>, T. J. Jones<sup>10</sup>,  
E. Perlman<sup>11</sup>

<sup>1</sup>Department of Physics & Astronomy, University of Texas at San Antonio, One UTSA Circle, San Antonio, TX 78249, USA.

<sup>2</sup>Department of Astronomy, University of Florida, 211 Bryant Space Science Center, P.O. Box 11205, Gainesville, FL 32611-2055, USA.

<sup>3</sup>Centre for Astrophysics Research, Science & Technology Research Institute, University of Hertfordshire, Hatfield, AL10 9AB, UK.

<sup>4</sup>Department of Physics and Astronomy, University of Kentucky, Lexington, KY 40506, USA.

<sup>5</sup>Gemini Observatory, Southern Operations Center, c/o AURA, Casilla 603, La Serena, Chile.

<sup>6</sup>Gemini Observatory, Northern Operations Center, 670 N. A'ohoku Place, Hilo, HI 96720.

<sup>7</sup>Instituto de Astrofísica de Canarias, C/ Vía Láctea, s/n, E-38205, La Laguna, Tenerife, Spain.

<sup>8</sup>Departamento de Astrofísica, Universidad de La Laguna, E-38205, La Laguna, Tenerife, Spain.

<sup>9</sup>Instituto de Física de Cantabria, CSIC-Universidad de Cantabria, 39005 Santander, Spain.

<sup>10</sup>Department of Astronomy, University of Minnesota, 116 Church Street S.E., Minneapolis, MN 55455, USA.

<sup>11</sup>Department of Physics and Space Sciences, 150 W. University Blvd., Florida Institute of Technology, Melbourne, FL 32901, USA

Accepted by MNRAS. Accepted 2013 February 25. Received 2013 February 11; in original form 2012 December 05

## ABSTRACT

An optically and geometrically thick torus obscures the central engine of Active Galactic Nuclei (AGN) from some lines of sight. From a magnetohydrodynamical framework, the torus can be considered to be a particular region of clouds surrounding the central engine where the clouds are dusty and optically thick. In this framework, the magnetic field plays an important role in the creation, morphology and evolution of the torus. If the dust grains within the clouds are assumed to be aligned by paramagnetic alignment, then the ratio of the intrinsic polarisation and visual extinction,  $P(\%)/A_v$ , is a function of the magnetic field strength.

To estimate the visual extinction through the torus and constrain the polarisation mechanisms in the nucleus of AGN, we developed a polarisation model to fit both the total and polarised flux in a  $1.2''$  ( $\sim 263$  pc) aperture of the type 2 AGN, IC5063. The polarisation model is consistent with the nuclear polarisation observed at  $K_n$  ( $2.0 - 2.3 \mu\text{m}$ ) being produced by dichroic absorption from aligned dust grains with a visual extinction through the torus of  $48 \pm 2$  mag. We estimated the intrinsic polarisation arising from dichroic absorption to be  $P_{K_n}^{\text{dic}} = 12.5 \pm 2.7\%$ .

We consider the physical conditions and environment of the gas and dust for the torus of IC5063. Then, through paramagnetic alignment, we estimate a magnetic field strength in the range of  $12 - 128$  mG in the NIR emitting regions of the torus of IC5063. Alternatively, we estimate the magnetic field strength in the plane of the sky using the Chandrasekhar-Fermi method. The minimum magnetic field strength in the plane of the sky is estimated to be  $13$  and  $41$  mG depending of the conditions within the torus of IC5063. These techniques afford the chance to make a survey of AGN, to investigate the effects of magnetic field strength on the torus, accretion, and interaction to the host galaxy.

**Key words:** AGN, torus – infrared: polarimetry.

## 1 INTRODUCTION

\* E-mail: elr@astro.ufl.edu

† Augusto Gonzalez Linares Senior Research Fellow

The detection of polarised broad emission lines in the spectrum of NGC1068 revealed an obscured Active Galactic Nu-

cleus (AGN) through scattering of the broad line region (BLR) radiation (Antonucci & Miller 1985). This study gave a major boost to the unified model (Antonucci 1993; Urry & Padovani 1995) of AGN, which holds that all AGN are essentially the same object, viewed from different line of sight (LOS). In the unified model scheme, the AGN classification solely depends on the obscuration of an optically and geometrically thick dusty torus

Recent studies (e.g. Nenkova et al. 2002, 2008) have proposed that the dust in the torus is distributed in clumps, and accounts for (a) the distribution of temperatures along the torus; and (2) the variety of spectral energy distributions (SED) produced by geometry, clumpy distribution and spectral features, such as the  $10\ \mu\text{m}$  absorption and emission. The clumpy torus model holds that the dusty clumps are distributed in a few parsecs, consistent with observations (e.g. Radomski et al. 2002; Jaffe et al. 2004; Packham et al. 2005; Suganuma et al. 2006; Tristram et al. 2007). This means that the torus cannot be resolved at optical/infrared (IR) wavelengths, even with the high-spatial resolution provided by 8-m class telescopes. Recent high-spatial resolution observations of Seyfert galaxies have shown that the clumpy torus model can account for the near-IR (NIR) and mid-IR (MIR) emission (see Mason et al. 2006; Ramos Almeida et al. 2009, 2011; Alonso-Herrero et al. 2011). Some studies (Mor, Netzer, & Elitzur 2009; Mor & Netzer 2012) have shown that a component composed by hot graphite dust can explain the NIR emission of Type 1 AGN. The clumpy torus models permit, from a statistical view, an examination of the general properties of the torus, i.e. inclination to our LOS, number of clouds, covering factor, optical depth of clouds, etc. However, the intrinsic properties of the clumpy torus, i.e. the dust grain composition, grain size, grain alignment, etc. remain unknown. Polarimetry techniques show a powerful potential to obtain the intrinsic properties of the torus. Several polarimetric studies in the IR to NGC1068 (Mason et al. 2007; Packham et al. 2007) have demonstrated this potential, constraining (1) interstellar dust properties; (2) upper-limit diameter of the torus; (3) mechanisms of polarisation and hence magnetic field directions in the central few pc.

Several models to explain the existence of the torus have been proposed. Some models explain the torus as an inflow of gas from large scales (e.g. Wada et al. 2009; Schartmann et al. 2011). Wada et al. (2009) presented numerical simulations of the interstellar medium to track the formation of molecular hydrogen forming an inhomogeneous disc around the central engine, identified as the torus. Schartmann, Krause, & Burkert (2011) suggested the origin of the torus as clouds falling to the central engine. In this scheme, it is difficult to explain how the energy dissipation of clouds and cloud-cloud collision tends to concentrate the clouds to form the torus near the midplane (Krolik & Begelman 1988). Conversely, some models (Blandford & Payne 1982; Emmering et al. 1992; Elitzur & Shlosman 2006) suggest that the clouds are confined by the magnetic field generated in the central engine and are accelerated by the hydromagnetic wind. In this scheme, the hydromagnetic wind could lift the clouds from the midplane to form a geometrically thick distribution of clouds surrounding the central engine, where the torus is in a particular region of the hydromagnetic wind where the clouds are dusty and optically thick. Kartje et al.

(1999) suggests that magnetic field strengths greater than 20 mG can account for a clumpy disc-driven wind model, where clouds move along the magnetic field lines in a homogeneous outflow component. VLA circular polarimetry observations of NGC4258 inferred an upper-limit of the magnetic field strengths of 300 mG (Herrnstein et al. 1998). Further polarimetric observations (Modjaz et al. 2005) at 22GHz of the water vapour maser clouds in NGC4258 using the VLA and GBT, estimate magnetic field strength from 90 to 300 mG at a radius of 0.2 pc from the central engine. In summary, observations and theoretical models for maser clouds at distances  $\sim 0.2$  pc seems to be in agreement. However, observational or theoretical studies at larger distances, where the clouds are optically thick and dusty, have not been done to date.

The nearby ( $z = 0.01^1$ ; de Vaucouleurs et al. (1991)) elliptical galaxy ( $r^{1/4}$  brightness profile; Colina et al. (1991)) IC5063 (PKS 2048-572) shows polarised scattered  $H_\alpha$  broad emission lines suggesting a hidden Type 1 AGN (Inglis et al. 1993), and an increase in the degree of polarisation in the infrared at J, H and K (Hough et al. 1987). A prominent dust lane has been observed (Colina, Sparks, & Macchetto 1991) along the long-axis of IC5063. IC5063 shows a radio luminosity ( $\log P_{1.4\text{GHz}} = 23.8\ \text{W Hz}^{-1}$ ,  $H_0 = 50\ \text{km s}^{-1}\ \text{kpc}^{-1}$ , Colina, Sparks, & Macchetto (1991)) about two orders of magnitude larger than is typical nearby Seyfert galaxies, classify IC5063 in the range of low-luminosity radio elliptical galaxies. The central polarised source have been suggested to be a BL Lac object from infrared observations by Hough et al. (1987). They showed a steep-spectrum IR component and suggested a synchrotron central source. Further NIR studies at J, H and K bands by Brindle et al. (1990) modeled the total and polarised flux of IC5063, and concluded that the nuclear source can be explained by a red-den central source with an power-law index of 1.5 (typical for Seyfert 1).

In this paper we estimate the magnetic field strength in the NIR emitting regions of the torus of AGN, through NIR polarimetric observations of IC5063 in the J, H and  $K_n$  bands. We develop a polarisation model to simultaneously fit the total and polarised flux, that allow us to interpret the different mechanisms of polarisation to the central engine of IC5063. Further estimates of the extinction to the central engine at different wavelengths allow us to interpret the origin of the NIR polarisation. Finally, four independent methods of calculating the magnetic field strength in the clumpy torus of IC5063 are presented.

The paper is structured as follow. In Section 2, we describe the observations and data reduction. In Section 3, the results are shown, then analysed in Section 4. We discuss various mechanisms of polarisation that could account for the polarisation in the nucleus of IC5063 and we develop a polarisation model to interpret our data in Section 5. In Section 6, the nuclear extinction estimated at various wavelengths is discussed. In Section 7, the magnetic field strength of the torus of IC5063 is estimated. Finally, conclusions are presented in Section 8.

<sup>1</sup> Through this work, we adopt  $H_0 = 73\ \text{km s}^{-1}\ \text{kpc}^{-1}$ , so that  $1'' = 219\ \text{pc}$  for the redshift of IC5063

## 2 OBSERVATIONS AND DATA REDUCTION

The observations were made using the infrared polarimeter built by the University of Hertfordshire (Hough et al. 1994) for the Anglo-Australian Telescope (AAT). The polarimeter features consist of an achromatic (1 - 2.5  $\mu\text{m}$ ) half-wave plate (HWP) retarder from 1.0 to 2.5  $\mu\text{m}$ , which can be stepped to set angular positions. This is placed upstream of the observatory's near-infrared camera, IRIS (Gillingham & Lankshear 1990), in which a magnesium fluoride Wollaston prism was used as an analyser. A mask in the focal plane of IRIS served to blank out half of the field so that the ordinary (o-ray) and extraordinary (e-ray) ray from Wollaston prism do not overlap when imaging extended objects as well as reduce the sky from overlapping.

IC5063 was observed on 1994 July 25, in the J, H and  $K_n$  (2.0 - 2.3  $\mu\text{m}$ ) bands, with IRIS at the f/15 focus using the Rockwell camera with  $128 \times 128$  pixels. The pixel-scale is 0.6'' per pixel, giving a field of view of  $76'' \times 76''$ . The half-wave retarder was stepped sequentially to four position angles (PA; 0°, 45°, 22.5° and 67.5°) taking an exposure at each HWP PA. Images at each HWP PA were flat-fielded, sky-subtracted and then cleaned by interpolating over dead and hot pixels and cosmic rays. Next, the images were registered and shifted by fractional pixel amounts in order to account for slight image drift between frames. Then, the polarisation images were constructed using our own IDL routines. The individual o- and e-ray images were co-averaged to increase the signal-to-noise ratio. Next, the o- and e-rays were extracted using a rectangular aperture of  $28'' \times 18''$ . The Stokes parameters, I, Q and U, were calculated according to the ratio method prescription (see Tinbergen (1996)). Finally, the degree of polarisation, P, was derived such as:

$$P = 100 \times \frac{\sqrt{Q^2 + U^2}}{I}$$

and the position angle of polarisation,  $\theta$ , was found by:

$$\theta = \frac{1}{2} \tan^{-1} \left( \frac{U}{Q} \right)$$

A summary of observations is shown in Table 1. The night was photometric with the seeing estimated to be 1.2'' from the automatic-guide at the observatory. Flux standard stars were not observed during this night, so we used the photometric data from Axon et al. (1982). Specifically, the flux calibration was performed using photometry at J, H and K in a 10'' aperture, where the large aperture ensures that centering issues are minimal. The difference between the K and  $K_n$  bands makes a small contribution to the total photometric error. The zero-flux standard values (Campins et al. 1985) of 1603 Jy, 1075 Jy and 667 Jy for J, H and  $K_n$ , respectively were used to transform between magnitudes and fluxes. To calibrate the PA of polarisation at J, H and  $K_n$ , a 4.5'' aperture from Hough et al. (1987) was used. Since unpolarised standard stars were unavailable, an instrumental polarisation of  $0.02 \pm 0.06\%$ , from previous studies by Hough et al. (1994) was adopted.

**Table 1.** Summary of observations.

Filter	Frame Time (s)	Sets	Total observation time (s)
J	30	12	1440
H	20	8	640
$K_n$	10	8	320

**Table 3.** The observed degree and position angle of polarisation and photometry of IC5063.

Aperture (")	Filter	P (%)	$\theta$ (°)	Magnitude
1.2	J	$2.0 \pm 0.7$	$0 \pm 2$	$14.81 \pm 0.02$
	H	$2.5 \pm 0.9$	$5 \pm 8$	$13.90 \pm 0.02$
	$K_n$	$7.8 \pm 0.5$	$4 \pm 4$	$13.01 \pm 0.06$
2.0	J	$1.5 \pm 0.5$	$-1 \pm 2$	$13.88 \pm 0.02$
	H	$2.0 \pm 1.6$	$4 \pm 11$	$12.95 \pm 0.02$
	$K_n$	$6.2 \pm 0.3$	$4 \pm 3$	$12.26 \pm 0.03$
3.0	J	$1.1 \pm 0.3$	$2 \pm 4$	$13.28 \pm 0.01$
	H	$1.6 \pm 0.9$	$3 \pm 7$	$12.38 \pm 0.01$
	$K_n$	$4.7 \pm 0.3$	$4 \pm 2$	$11.79 \pm 0.02$
4.0	J	$0.9 \pm 0.2$	$5 \pm 5$	$12.89 \pm 0.01$
	H	$1.1 \pm 0.5$	$3 \pm 6$	$12.01 \pm 0.01$
	$K_n$	$3.8 \pm 0.1$	$4 \pm 2$	$11.48 \pm 0.01$

## 3 RESULTS

### 3.1 Photometry

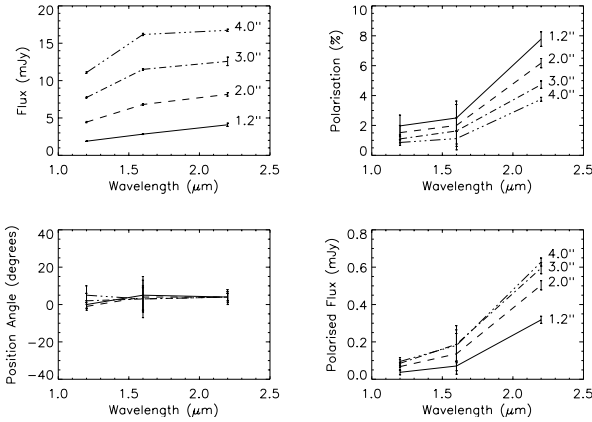
We made measurements of the nuclear total flux in several apertures to compare to previously published values (Table 2). In all cases, photometric errors were estimated by the variation of the counts in subsets of the data. The difference in fluxes between our and previously published results is  $< 4\%$  in all apertures. To optimally measure the AGN flux of IC5063 and minimize the contributions from the host galaxy, dust lane and ionisation cones, photometry in an aperture equal to the seeing of the observations (1.2'') was used. To investigate the flux dependence on the aperture size, photometry in three apertures, 2.0'', 3.0'' and 4.0'', was measured (Table 3). An increase in total flux at both longer wavelengths and larger aperture was found (Figure 1). In line with previous studies, an elliptical profile with a FWHM of  $3.7'' \times 2.6''$ ,  $3.4'' \times 2.5''$  and  $2.3'' \times 1.8''$  at J, H and  $K_n$  respectively, was found for the nucleus of IC5063. In all filters, IC5063 was found to be extended along PA = 75°. The FWHM was estimated using a Gaussian profile.

### 3.2 Polarimetry

We made measurements of the nuclear degree of polarisation in several apertures to compare to previously published values (Table 2). In all cases, polarimetric errors were estimated by the variation of the counts in subsets of the data. The observed degree and PA of polarisation in four different sized apertures, 1.2'', 2.0'', 3.0'', 4.0'', were measured (Table 3). Polarimetry maps of the total and polarised flux are shown in Figures 2 and 3 in J, H and  $K_n$  bands. In these figures, the overlaid polarisation vectors are proportional in length to the degree of polarisation with their orientation

**Table 2.** Comparison with literature of the nuclear photometry of IC5063.

Aperture ( $''$ )	Filter	Hough et al. (1987) Mag (mag)	P (%)	This work Mag (mag)	P (%)
2.25	H	12.38	$1.75 \pm 0.34$	$12.86 \pm 0.02$	$1.8 \pm 1.5$
	K <sub>n</sub>	11.79	$6.33 \pm 0.50$	$12.18 \pm 0.02$	$6.0 \pm 0.3$
4.5	J	12.50	$0.77 \pm 0.07$	$12.71 \pm 0.01$	$0.7 \pm 0.2$
	H	11.80	$0.99 \pm 0.05$	$11.83 \pm 0.01$	$1.0 \pm 0.4$
	K <sub>n</sub>	11.10	$3.25 \pm 0.45$	$11.34 \pm 0.01$	$3.3 \pm 0.1$
Aperture ( $''$ )	Filter	Axon et al. (1982) Mag (mag)	This work Mag (mag)		
5.0	J	12.72	$12.59 \pm 0.01$		
	H	11.80	$11.72 \pm 0.01$		
	K <sub>n</sub>	11.32	$11.23 \pm 0.01$		

**Figure 1.** Total flux (*top left*), degree (*top right*) and position angle (*bottom left*) of polarisation and polarised flux (*bottom right*) versus wavelength. Measurements with aperture size of 1.2'' (solid line), 2.0'' (dashed line), 3.0'' (dashed dotted line) and 4.0'' (dashed three-dotted line) are shown in each plot.

showing the PA of polarisation. The lowest-level total flux contour indicates the level at which 0.8% of uncertainty in polarisation is reached. The polarised flux images at J, H and K<sub>n</sub> are shown in Figure 4.

At J, we interpret the extended polarisation in the central regions to be dichroic polarisation of starlight through aligned dust grains in the host galaxy and the central dust lane (Colina, Sparks, & Macchetto 1991). The patchy distribution of dust in the nuclear regions results in a polarisation dependence with aperture size. At H, the most striking feature is the polarisation vector pattern (Figures 2 and 3) and the extended structure seen in polarised flux (Figure 4). The polarised structure is extended  $\sim 3''$  from NW to SE along of a PA  $\sim 300^\circ$ . The strong spatial correspondence with the structure at 8GHz of a PA of  $295^\circ$  (Morganti, Oosterloo, & Tsvetanov 1998), and the “X-shape” in the [OIII] observations at PA of  $290^\circ$  (Colina, Sparks, & Macchetto 1991) are shown in Figure 5. The polarised flux images show a tentative opening angle of  $\sim 75^\circ$  at the H band, larger than

the  $60^\circ$  measured through the [OIII] ionised structure by Colina, Sparks, & Macchetto (1991). We note that other AGN show a wider opening angle in polarised flux than emission line imaging, e.g. NGC1068 has an opening angle of  $60^\circ \pm 20^\circ$  from [OIII] imaging (Evans et al. 1991) and  $80^\circ$  from NIR polarimetry imaging (Packham et al. 1997). The opening angle in polarised light is larger because of scattering can occur from any material in the medium, instead, the medium needs to be filled by [OII], in order to be ionised ([OIII]), producing a smaller opening angle. We interpreted the biconical polarised distribution to be scattering of light from the central engine to our LOS. At K<sub>n</sub>, a highly polarised point-like source is observed.

The polarisation of the central 1.2'' of IC5063 at J, H and K<sub>n</sub> was measured to be  $2.0 \pm 0.7\%$ ,  $2.5 \pm 0.9\%$  and  $7.8 \pm 0.5\%$ , respectively. Figure 1 shows that the degree of polarisation decreases as the aperture size increases in all filters, whereas the polarised flux remains similar in the 3'' and 4'' apertures at J and H. Finally, the PA of polarisation is wavelength-independent (within the error bars) and measured to be  $3 \pm 6^\circ$  in the three filters. This result is consistent with the PA of polarisation of  $3 \pm 2^\circ$  measured by Hough et al. (1987) in the J, H and K filters, and  $\sim 3^\circ$  using optical (0.45 - 0.70  $\mu\text{m}$ ) spectropolarimetry by Inglis et al. (1993). Note that the PA of polarisation,  $3 \pm 6^\circ$ , is perpendicular to (1) the long-axis,  $300^\circ$ , of the galaxy (Colina et al. 1991); and (2) the radio-axis,  $295^\circ$  (Morganti, Oosterloo, & Tsvetanov 1998).

## 4 ANALYSIS

The measured polarisation is the diluted polarised light from the AGN produced by the diffuse stellar emission. Hence, the intrinsic polarisation can be estimated accounting for the contributions by the AGN and diffuse stellar emission to the total flux in the nucleus of IC5063. We quantify these contributions through an examination of the nuclear profiles in Section 4.1.

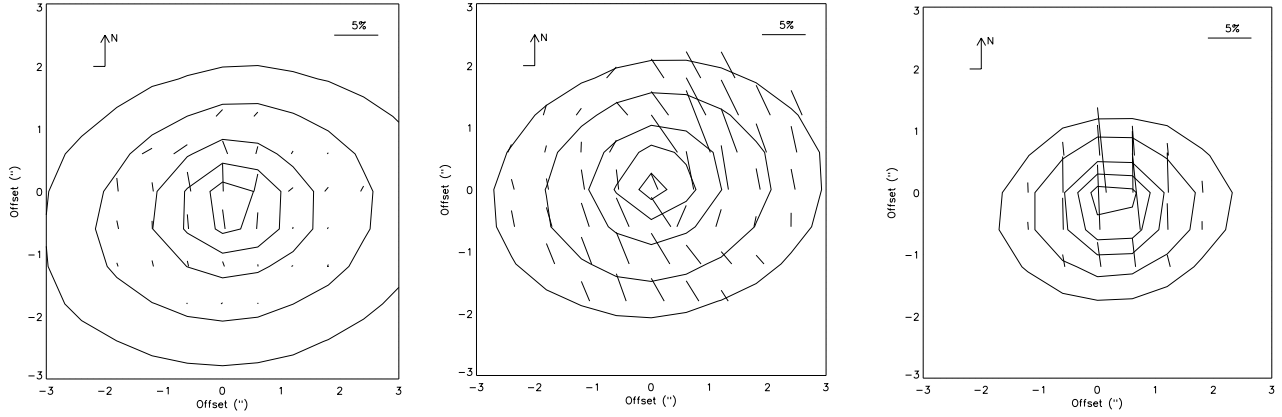


**Figure 2.** Total flux contours with polarisation vectors of the central  $6'' \times 6''$  at J (*left*), H (*middle*) and  $K_n$  (*right*). A vector of 5% of polarisation is shown at the top right of each plot. The lowest-level total flux contour represents an uncertainty of 0.8% in the degree of polarisation. Contours are plotted in intervals of 10% to the peak of the total flux at each band. North is up and East left. The physical scale is  $1'' = 219$  pc.

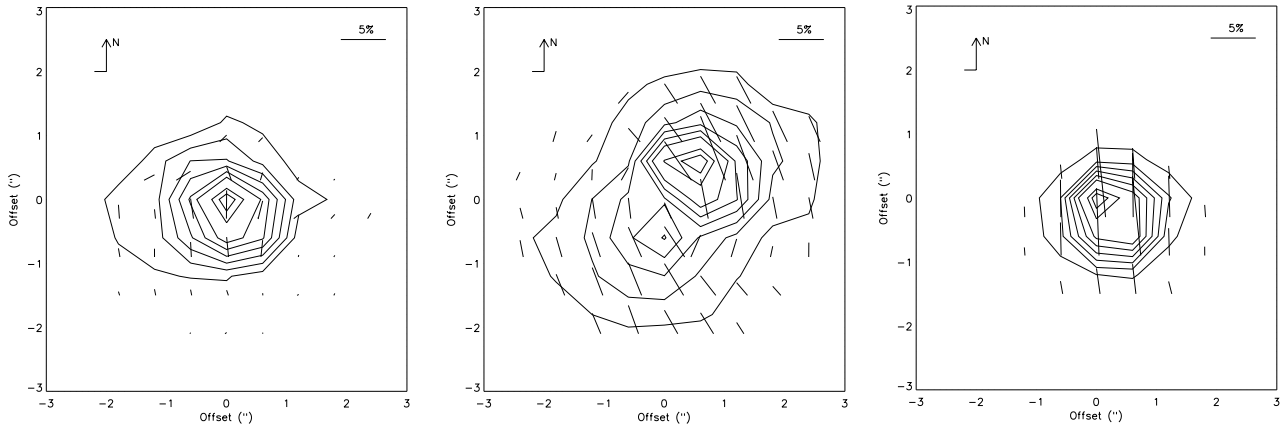


**Figure 3.** Polarised flux contours with polarisation vectors of the central  $6'' \times 6''$  at J (*left*), H (*middle*) and  $K_n$  (*right*). A vector of 5% of polarisation is shown at the top right of each plot. Contours are plotted in intervals of 10% to the peak of the polarised flux at each band. North is up and East left. The physical scale is  $1'' = 219$  pc.

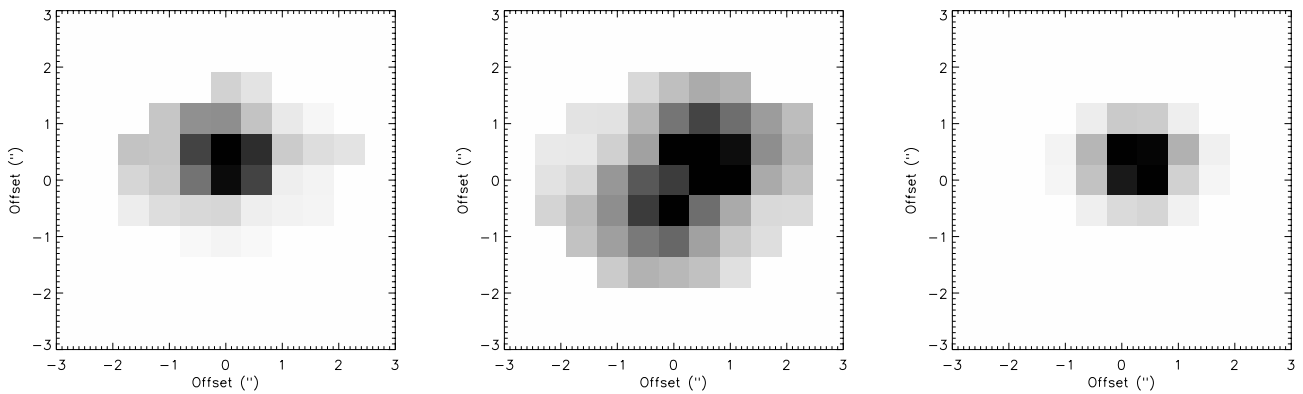


**Figure 4.** Polarised flux images of the central  $6'' \times 6''$  at J (*left*), H (*middle*) and  $K_n$  (*right*) bands. North is up and East is left. The physical scale is  $1'' = 219$  pc.

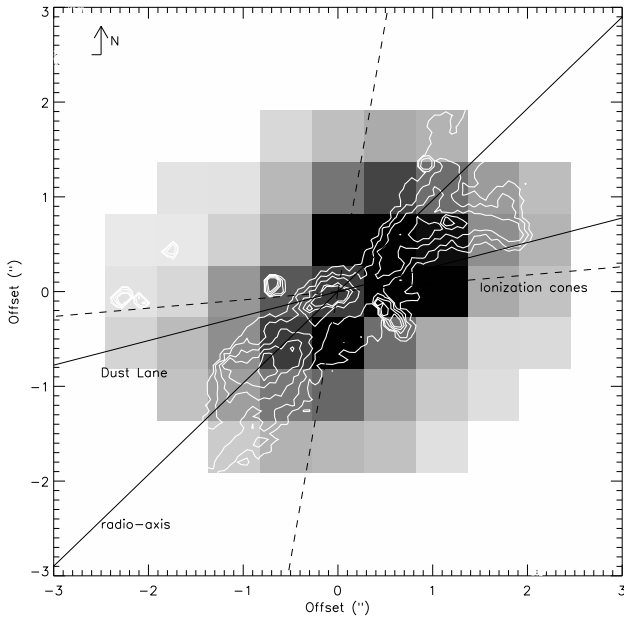


**Figure 5.** Polarised flux at H (grey scale). [OIII] ionisation structure from HST by Schmitt et al. (2003) (contours). Radio-axis with  $PA \sim 295^\circ$  is shown (Morganti et al. 1998). Dust lane axis with  $PA = 75^\circ$ , from Colina, Sparks, & Macchetto (1991). Polarised cones axis (dashed line) with opening angle of  $75^\circ \pm 5^\circ$  are from this paper. The physical scale is  $1'' = 219$  pc.

#### 4.1 The nuclear total flux

The AGN is embedded within diffuse stellar emission in the nuclear bulge. The emission within the nuclear regions of IC5063 can be considered to arise from two dominant emission components: (1) diffuse stellar emission in the nuclear bulge; and (2) emission from the AGN. Photometric cuts through the nucleus in the J band show no evidence of a nuclear point-source, and hence we assume that there is negligible emission from the AGN in our smallest aperture ( $1.2''$ ;  $\sim 263$  pc). Thus, the J band profile is assumed to be representative of the profile of the diffuse stellar emission in the nuclear bulge. However, at  $K_n$  we detect both a central point-source and emission from the diffuse stellar bulge. We interpret the central point-source emission to be the AGN. To estimate the relative contributions from these two emission components, two different methods were followed. In the first method, we followed a similar analysis to that of Turner et al. (1992) and Packham et al. (1996). We took photometric cuts at J and  $K_n$  along the dust lane axis,  $PA = 75^\circ$  (Colina, Sparks, & Macchetto 1991). These cuts are assumed to be along a line of constant extinction through the nucleus ( $A_V = 0.3$  mag; Colina, Sparks, & Macchetto (1991)). The AGN contribution, modeled as a point-source convolved with a Gaussian profile of FWHM equal to that of the seeing disc, is termed  $AGN_{PSF}$ . To fit the  $K_n$  nuclear bulge profile along the cut, the emission was modeled as the summation of the  $AGN_{PSF}$  and the diffuse stellar emission from the J band photometric profile. The photometric profiles in J,  $K_n$ , the modeled  $AGN_{PSF}$  and the combined J and  $AGN_{PSF}$  to fit the  $K_n$ -profile are shown in Figure 6, showing an acceptable fit to the data. Through this method, the best estimate of the contribution of the AGN emission

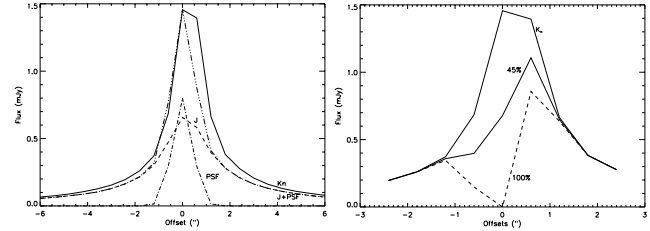


**Figure 6.** Cuts profile for the first method in Section 4.1 are shown (left panel). Cuts profiles at J (dashed line),  $K_n$  (solid line) and the scaled  $AGN_{PSF}$  (dashed dotted line). The combined J profile and  $AGN_{PSF}$  matched with the  $K_n$ -profile (thick dashed three-dotted line). “Flat-top” profile for the second method in Section 4.1 are shown (right panel). Same  $K_n$  profile than in left panel (solid line) and the subtraction of the  $AGN_{PSF}$ -scaled at 45% (thick solid line) and 100% (dashed line).

to the total flux is  $40 \pm 2\%$  in a  $1.2''$  aperture. This result is comparable to that determined for Centaurus A,  $\sim 30\%$  AGN contribution, when using a similar methodology by Packham et al. (1996).

In the second method, the scaled  $AGN_{PSF}$  from the first method was used to subtract the AGN emission from the  $K_n$  image. This procedure produces a “flat-top” profile over the center (Figure 6), which likely leads to a modest overestimation of the AGN contribution as the underlying stellar emission will peak at or very close to the AGN emission peak (for examples of this technique, see Radomski et al. 2002, 2003; Ramos Almeida et al. 2009; Levenson et al. 2009). Then, flux of the  $AGN_{PSF}$ -subtracted  $K_n$  image is measured to be 2.25 mJy (13.66 mag.) in a  $1.2''$  aperture. Diffuse stellar emission in the nuclear bulge has a contribution of  $55 \pm 3\%$  ( $45 \pm 3\%$  AGN emission) as measured through this second method.

From the methods presented above, the average of the AGN emission is estimated to be  $43 \pm 3\%$ , whereas the contribution from the diffuse stellar emission in the nuclear bulge is estimated to be  $57 \pm 3\%$ , both estimated in a  $1.2''$  aperture. The formal uncertainties are estimated to be 5% from photometric measurements. Systemic errors from this methodology could increase the final uncertainties, but are difficult to quantify. Previous observations (Kulkarni et al. 1998) at  $1.1 \mu m$ ,  $1.6 \mu m$  and  $2.2 \mu m$  using NICMOS/HST showed an unresolved point-source, consistent with an obscured AGN. Kulkarni et al. (1998) suggested that the infrared emission at  $2.2 \mu m$  is dominated by thermal emission from hot ( $T = 720$  K) dust in the inner edge of the torus. They suggested that the 75% of the flux at  $1.6 \mu m$  is due to emission other than hot dust in the inner edge of the torus, consistent with that only diffuse stellar emission contributes to the total flux at shorter wavelengths, H band.

#### 4.2 The nuclear intrinsic polarisation

The diffuse stellar emission in the nuclear regions of IC5063 significantly dilutes the observed emission from the AGN, as estimated in Section 4.1. We subtracted the diffuse stellar emission in the measured degree of polarisation at  $K_n$  in a  $1.2''$  aperture, and an intrinsic polarisation of  $P_{K_n}^{int} = 18.1 \pm 1.1\%$  was estimated. Note that the intrinsic polarisation calculated here is independent of the polarising mech-

anisms of the central engine. The estimated intrinsic polarisation is in good agreement with previous NIR studies at J, H and K<sub>n</sub> by Hough et al. (1987), where an intrinsic polarisation of  $17.4 \pm 1.3\%$  was calculated, using their own photometric data and photometry from Axon et al. (1982) in the H and K filters using a  $2.25''$  aperture. Brindle et al. (1990) used the same data of Hough et al. (1987) and with slightly different assumptions calculated an intrinsic polarisation of  $15.3 \pm 1.0\%$  in a  $2.25''$  aperture. They used a polarised power-law component and starlight subtraction. Optical spectropolarimetric studies by Inglis et al. (1993) estimated an intrinsic polarisation of  $\sim 10\%$ , based on narrow lines in the range of  $0.54 - 0.70 \mu\text{m}$ . Studies of other AGN have shown highly intrinsic polarised nucleus. For example, Simpson et al. (2002) measured a polarisation of 6% in the nucleus of NGC1068 and Tadhunter et al. (2000) estimated an highly intrinsic polarisation of  $>28\%$  in the nucleus of Cygnus A, where both observations used the  $2 \mu\text{m}$  polarimetry mode of NICMOS/HST.

## 5 POLARISATION MODEL

To investigate the polarisation from the torus, the aligned dust grains and the role of magnetic fields, we developed a polarisation model to take into account the various mechanisms of polarisation in the nuclear regions of IC5063. In the sections below, we discuss the possible mechanisms of polarisation and then we construct a polarisation model.

### 5.1 Possible mechanisms of polarisation

We consider that the nuclear polarisation could arise through three mechanisms in the NIR: (1) synchrotron radiation, as suggested by Hough et al. (1987) from a central BL Lac type object; (2) dichroic absorption by galactic nuclear dust and the torus; and/or (3) scattering of nuclear radiation, as indicated by the ionisation cones.

#### 5.1.1 Synchrotron emission

Optical and NIR polarimetric observations of IC5063 by Hough et al. (1987) suggested that the large intrinsic degree of polarisation,  $17.4 \pm 1.3\%$ , arises from a non-thermal nuclear source. The intrinsic polarisation is comparable with previous observations of BL Lac objects (Angel et al. 1978; Bailey et al. 1983) and is generally attributed to synchrotron emission mechanism. BL Lac objects are observed to show a high degree of photometric variability with times-scales of weeks and a factor of two in amplitude in the optical UBV filters (Impey & Neugebauer 1988). NIR (J, H and K bands) variation, when detect at all, are smaller and longer time-scale than in optical (Neugebauer et al. 1989; Hunt et al. 1994). IC5063 does not show any significant flux-variability versus time (Colina, Sparks, & Macchetto 1991), because we are using previous data for calibration, we cannot comment further on the issue of variability for IC 5063. However, the optical (Inglis et al. 1993) and NIR (Hough et al. 1987, this paper) polarisation shows a wavelength-dependence on the intrinsic polarisation, that is not inconsistent with a synchrotron source. A further argument against a synchrotron origin for the observed NIR polarisation is that the polarised

radio emission in IC 5063 (Morganti et al. 2007) is located  $1'' - 2''$  SW of the nucleus, with polarisation vectors oriented along a very different direction that what we observe in the nucleus (Figures 1 and 2). A decisive test of the synchrotron emission interpretation is mm polarisation measurements, but as yet no such observations have been published. The lack of total flux variability strongly argues against synchrotron being a dominant emission mechanism. Hence, we do not consider that the polarisation arises dominantly from synchrotron mechanism.

#### 5.1.2 Dichroic absorption

Young et al. (1995) showed that the polarisation at K is attributed to dichroic absorption of the central engine radiation passing through the dust within the torus with visual extinction  $\geq 45$  mag in NGC1068. They argued that the increase in the degree of polarisation with wavelength is due to dichroic absorption in the NIR. As example, Simpson et al. (2002) measured a level of polarisation of 6% in the unresolved nucleus of NGC1068 at  $2 \mu\text{m}$  using NICMOS/HST. They argued that the polarisation is likely produced by dichroic absorption arising from the molecular clouds associated with the torus. Hence, the visual extinction of  $\geq 45$  mag. is consistent with measurements of the degree of polarisation of 6%. For detailed discussion of the extinction to the nucleus of IC5063 at several wavelengths see Section 6. To study how dichroism affects the polarisation in the unresolved nucleus of IC5063, this mechanism is included in the polarisation model.

#### 5.1.3 Scattering

Broad emission lines in polarised flux have been detected in the optical spectrum of IC5063 (Inglis et al. 1993), which strongly implies the presence of a nuclear dust and/or electron scattering screen. Indeed, our observations show, for first time in polarised flux in IC5063, the dual-ionisation cones at H (Figure 5), arising from scattering of nuclear radiation by agents within the ionisation cones. At J, the ionisation cones are not observed as (a) the counter (rear projected) cone is obscured by the dusty disc of the host galaxy; and (b) the forward (front projected) cone's polarised flux is not clearly detected due to host galaxy contamination and/or low signal to noise in the cone area. At K<sub>n</sub>, the cones are also not observed, as the signal-to-noise of our observations is insufficient to map the cones beyond the central  $2''$  aperture. To study how scattering affects the polarisation in the unresolved nucleus of IC5063, this mechanism is included in the polarising model.

To understand the polarisation mechanisms responsible for the compact nuclear polarisation and the wavelength dependencies, a polarisation model to simultaneously fit the total flux, polarised flux and the degree and PA of polarisation is developed and described in the following sections.

### 5.2 Total flux modeling

To estimate the visual extinction through the torus and constrain the polarisation mechanisms in the nucleus of AGN, we developed a polarisation model to fit both the total and

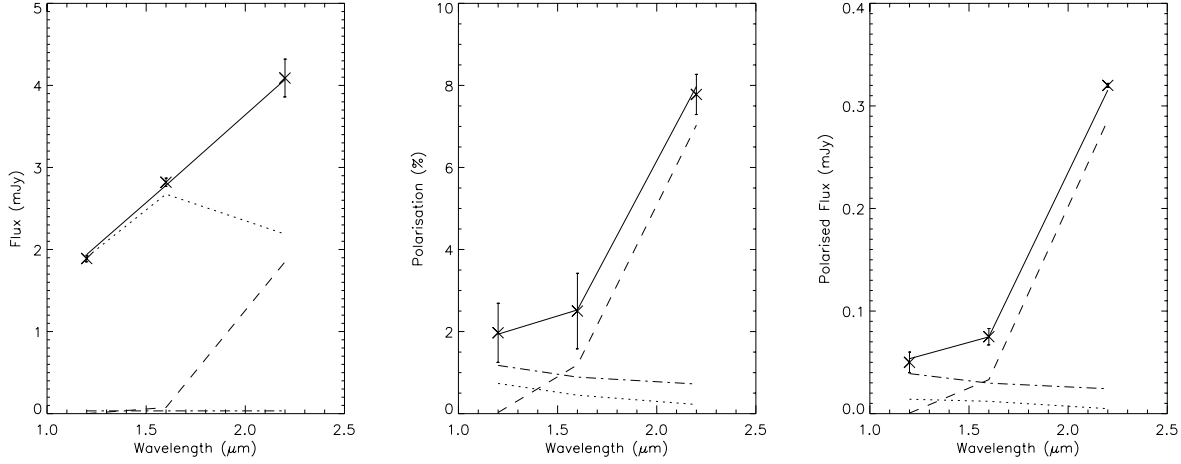


**Figure 7.** Model fit (Section 5) to the total flux in a  $1.2''$  aperture (*left panel*). The diffuse stellar emission through the nuclear bulge (*dotted line*), AGN through torus (*dashed line*), ionisation cones (*dashed dotted line*) and the total (*solid line*) are shown. Model fit to the degree of polarisation (*middle panel*) and polarised flux (*right panel*) in a  $1.2''$  aperture are shown. Polarisation produced through the dichroic absorption by the dust in the nuclear bulge (*dotted line*) and within the torus (*dashed line*), electron scattering (*dashed dotted line*) and total (*solid line*) are shown.

polarised flux in a  $1.2''$  ( $\sim 263$  pc) aperture of the type 2 AGN, IC5063.

The model consists of a point-source emitter, the central engine, partially extinguished by dust within the torus and the nuclear bulge. The central engine is described as an unpolarised power-law source, ( $F_\nu \propto \nu^{-\alpha}$ ), with an assumed power-law index,  $\alpha = 1.5$ , typical of Seyfert 1 nuclei and previously used for IC5063 (Brindle et al. 1990; Colina et al. 1991; Inglis et al. 1993). The power-law is partially extinguished by two contributions, one by dust in the torus,  $A_v(1)$ , and one by dust in the nuclear bulge,  $A_v(2)$ . We also included a contribution from the diffuse stellar emission in the nuclear bulge, modeled using typical starlight colors of elliptical galaxies,  $(J-H) = 0.75$  mag. and  $(H-K) = 0.22$  mag. (Sparks et al. 1986). The diffuse stellar emission in the nuclear bulge contribution to the total flux was constrained to be 57% at  $K_n$  in a  $1.2''$  aperture (Section 4.1). The diffuse stellar emission contribution was reddened by  $E(B-V) = 0.26$  mag., estimated from the  $(J-H)$  and  $(H-K_n)$  maps of IC5063. Similar values have been used in the literature, Inglis et al. (1993) used  $E(B-V) = 0.6$  mag., Colina et al. (1991) estimated  $E(B-V) = 0.1 - 0.4$  mag., and Brindle et al. (1990) used  $E(B-V) = 0.12$  mag., calculated by Boisson & Durret (1986). A range of  $E(B-V) = 0.2-0.6$  mag. was used by Bergeron et al. (1983). The reddening power-law,  $\tau_\lambda \propto \lambda^{-1.85 \pm 0.05}$  by Landini et al. (1984) was used.

An additional component added to the total flux to represent scattering within the NW and SE ionisation cones was also included. Both cones were (initially) assumed to suffer the same level of extinction from the nuclear bulge.

We fit the measured total fluxes in a  $1.2''$  aperture, by adjusting the visual extinctions,  $A_v(1)$  and  $A_v(2)$ , of the total flux model. The fit was considered acceptable when the deviation from the modeled J, H and  $K_n$  total fluxes was  $<1\%$  of the flux value at all wavelengths. Using this procedure, the fit to the total flux at J, H and  $K_n$  was obtained (Figure 7), giving a visual extinction of  $A_v(1) = 48 \pm 2$  mag.

and  $A_v(2) = 6 \pm 2$  mag. The visual extinction for the host galaxy,  $A_v(2)$ , is close to the previous determination,  $A_v = 7$  mag. by Heisler & De Robertis (1999). The total visual extinction to the central engine of IC5063 is  $A_v(1) + A_v(2) = 54 \pm 4$  mag., consistent with the extinction,  $A_v = 64 \pm 15$  mag., estimated using optical ( $[OIII]\lambda 5007$ ) and infrared (K and L') spectral index and visual extinction maps (Simpson et al. 1994). For the ionisation cones, the SE cone (counter-cone) was extinguished with the nuclear bulge visual extinction,  $A_v(2) = 6 \pm 2$  mag, while no extinction for the NW cone (forward-cone) was needed. This is entirely consistent with the NW cone being in front of the obscuration of the nuclear bulge.

### 5.3 Polarisation modeling

Using the same model, the wavelength-dependence of the observed polarised flux in the nuclear regions of IC5063 at J, H and  $K_n$  in a  $1.2''$  aperture was examined. The model assumes two separate polarising mechanisms. First, dichroic absorption by the interstellar medium of the central engine power-law emission. The interstellar polarisation follows a typical Serkowski curve (Serkowski, Mathewson, & Ford 1975):

$$\frac{P(\lambda)}{P_{\max}} = \exp \left[ -K \ln^2 \left( \frac{\lambda_{\max}}{\lambda} \right) \right]$$

where,  $P_{\max}$ , represents the maximum of polarisation at  $\lambda_{\max}$  and  $K = 0.01 \pm 0.05 + (1.66 \pm 0.99) \lambda_{\max}$  (Whittet et al. 1992).

Our polarimetric data and the optical and NIR polarimetric data from Hough et al. (1987) were used to fit the Serkowski curve. The best fit is  $P_{\max} = 1.4 \pm 0.1\%$ ,  $\lambda_{\max} = 0.50 \pm 0.02 \mu m$  and  $K = 0.84^{+0.14}_{-0.06}$ . These values are similar to  $P_{\max} = 1.49 \pm 0.08\%$  and  $\lambda_{\max} = 0.51 \pm 0.02 \mu m$ , previously estimated by Brindle et al. (1990) for IC5063.

NIR polarimetric studies have shown that the observed polarisation in the range of  $1.0-2.5 \mu m$  is better represented



by a power law  $P \propto \lambda^{-\gamma}$ , with  $\gamma$  in the range of 1.6-2.0 (e.g. Nagata 1990; Martin & Whittet 1990). The degree of polarisation arising from dichroic absorption through a dust column can be estimated by the knowledge of the extinction,  $A_\lambda$ , and observed polarisation power-law. Thus, we use the expected polarisation by a dust column given by  $P_\lambda \propto A_\lambda \times \lambda^{-\gamma}$ .

Second, wavelength-independent electron scattering,  $P = \lambda^0$ , is considered to be the polarising mechanism in the ionisation cones. Previous studies from UV to NIR (e.g. Antonucci & Miller 1985; Young et al. 1995; Inglis et al. 1993) have shown that electron scattering is the dominant polarising mechanism in the ionisation cones.

We fit the polarised flux, the degree and PA of polarisation using simultaneously the results of the previous section with the constraints given by (a) the intrinsic polarisation of  $P_{K_n}^{\text{int}} = 18.1 \pm 1.1\%$ ; (b) the visual extinction of  $A_v(1) = 48 \pm 2$  mag., and  $A_v(2) = 6 \pm 2$  mag.; and (c) a power-law index  $\gamma = 1.9$  (Figure 7). The fit was considered acceptable when the difference between the model and observed J, H and  $K_n$  polarised flux was  $< 1\%$ . Within the  $1.2''$  aperture, the polarised flux at J electron scattering (67%) and dichroic absorption from dust in the nuclear bulge (33%) are the dominant polarising mechanisms, with zero contribution of dichroic absorption within the torus. At H, the observed polarised flux is estimated to be 71% dichroic absorption from dust in the nuclear bulge, 16% dichroic absorption within the torus and 13% electron scattering. At  $K_n$ , the observed polarised flux produced through dichroic absorption within the torus is 89%, 8% electron scattering and 3% dichroic absorption from dust in the nuclear bulge.

#### 5.4 Intrinsic polarisation through dichroic absorption within the torus

The intrinsic polarisation calculated in Section 4.2 is independent of the polarising mechanisms to the central engine of IC5063. To estimate the intrinsic polarisation arising from dichroic absorption ( $P_{K_n}^{\text{dic}}$ ) through the torus, the measured polarisation,  $P_{K_n}^{\text{obs}} = 7.8 \pm 0.5\%$ , at  $K_n$  in a  $1.2''$  was corrected by accounting for (1) the measured degree of polarisation through dichroic absorption from dust in an off-nuclear region; (2) the estimated polarisation through dichroic absorption from dust in the nuclear bulge; (3) the fractional contribution of the central engine to the total flux; and (4) the fractional contribution of the dichroic absorption within the torus.

The degree of polarisation at  $K_n$  produced through dichroic absorption from dust in an off-nuclear region of IC5063 was measured to be  $P_{K_n}^{\text{off}} = 0.2\%$ , with a PA of polarisation  $\sim 15^\circ$ . Note that the difference in PA of polarisation at  $K_n$  between the nuclear ( $3 \pm 6^\circ$ ) and off-nuclear ( $\sim 15^\circ$ ), represents a lower-limit in the subtraction of the diffuse stellar emission in the nuclear bulge of IC5063, as polarisation is a vector (rather than a scalar) quantity.

The estimated polarisation produced through dichroic absorption from dust in the nuclear bulge is estimated by the relationship  $P(\%)/A_v = 1 - 3\% \text{ mag}^{-1}$  (Greenberg 1978; Whittet et al. 2001; Lazarian 2007). Using our estimated value of the nuclear bulge visual extinction,  $A_v(2) = 6 \pm 2$

mag (Section 5.2), transformed<sup>2</sup> to  $A_{K_n} = 0.7 \pm 0.2$  mag, the dichroic absorption polarisation from dust in the nuclear bulge at  $K_n$ , is calculated to be in the range of  $P_{K_n}^{\text{dic}} = 0.5 - 2.7\%$ .

The contributions of the AGN and diffuse stellar emission in total flux from Section 4.2 are  $43 \pm 3\%$  and  $57 \pm 3\%$ , respectively. We define the ratio of the diffuse stellar emission and AGN contribution to be  $\text{AGN}^{\text{ratio}} = 57 \pm 3\% / 43 \pm 3\%$ . Through the use of the polarisation model described above, the fraction of polarised flux produced through dichroic absorption within the torus is  $\text{AGN}_{K_n}^{\text{dic}} = 89\%$  at  $K_n$ .

The intrinsic polarisation arising from dichroic absorption ( $P_{K_n}^{\text{dic}}$ ) in the central  $1.2''$  aperture of IC5053 was estimated as:

$$P_{K_n}^{\text{dic}} = (P_{K_n}^{\text{obs}} - P_{K_n}^{\text{off}} - P_{K_n}^{\text{dic}}) \times (1 + \text{AGN}^{\text{ratio}}) \times \text{AGN}_{K_n}^{\text{dic}}(1)$$

The intrinsic polarisation at  $K_n$  produced by dichroic absorption within the torus is estimated to be  $P_{K_n}^{\text{dic}} = 12.5 \pm 2.7\%$ .

## 6 NUCLEAR EXTINCTION

The AGN is obscured by the torus and suffers further extinction from the host galaxy. Both extinctions were estimated using the simple NIR polarisation model described in Section 5. However, estimates at other wavelengths provide further constraints on the extinction to the torus. For example, X-ray wavelengths offer perhaps the optimal estimation of the absorption to the central engine of the AGN, whereas the  $9.7\text{-}\mu\text{m}$  silicate feature in the MIR affords the chance to investigate the cooler dust of the torus. In order to study the extinction at different wavelengths and its relation with the torus, the extinction to the nuclear point source was estimated through five different techniques, as described below.

(1) X-ray. The visual extinction to the nucleus of IC5063 can be calculated using the standard Galactic ratio  $A_v/N_H = 5.23 \times 10^{-22} \text{ mag cm}^2$  (Bohlin et al. 1978). Tazaki et al. (2011) calculated an atomic hydrogen column density of  $N_H = 25.0 \pm 0.7 \times 10^{22} \text{ cm}^{-2}$  from *Swift*/BAT data in the energy band of 0.5 - 200 keV. Hence, the visual extinction is estimated to be  $A_v = 131 \pm 4$  mag. A similar result of  $A_v = 115 \pm 20$  mag., was obtained by Simpson et al. (1994) using *Ginga* observations.

(2) NIR polarimetry. Jones (1989) and Jones, Klebe, & Dickey (1992) examined the relationship between the degree of polarisation and the optical depth at K as a function of the geometry of the magnetic field. They found that the best correlation between the degree of polarisation and the optical depth at K for stars extinguished by dust is  $P_K = 2.23 \tau_K^{3/4}$  (see equation 2 in Jones 1989). This model includes with equal contributions from random and constant component of the magnetic field. For the constant component of the magnetic field, the relationship between the degree of polarisation and the optical depth is  $P_K = \tanh \tau_p$  (see equation A7 in Jones 1989). In the case of IC5063, using the intrinsic polarisation arising from dichroic absorption within

<sup>2</sup> The conversion of visual extinction,  $A_v$ , to extinction at  $K_n$ ,  $A_{K_n}$ , is  $A_{K_n} = 0.112 A_v$  (Jones 1989).

the torus,  $P_{K_n}^{\text{dic}} = 12.5 \pm 2.7\%$ , and the conversion  $\tau_K = 0.09 A_v$  (Jones 1989), the visual extinction is calculated to be in the range of 22 - 111 mag. for constant component of the magnetic field; and equal contributions from random and constant component to the magnetic field, respectively. The visual extinction by the torus,  $A_v(1) = 48 \pm 2$  mag., estimated through the polarising model in Section 5, is within the visual extinction estimated from these two relationships.

(3) Silicate absorption. Using the empirical relation between the visual extinction and silicate absorption strength,  $A_v/\tau_{9.7\mu\text{m}} = 18.5 \pm 1.0$ , (Whittet 1987) and the silicate absorption,  $\tau_{9.7\mu\text{m}} = 0.32 \pm 0.02$ , measured from N-band spectra of the nucleus of IC5063 (Young et al. 2007), the visual extinction is calculated to be  $A_v = 6 \pm 1$  mag. This value presumably estimates not the extinction to the central engine, but the extinction to the outer region of the clumpy torus as the observed silicate feature presumably results from a mixture of emission and absorption within the torus, this should be considered a lower limit to the true extinction.

(4) Clumpy torus model. The visual extinction to our LOS,  $A_v^{LOS}$ , is calculated using the clumpy torus model (Nenkova et al. 2002, 2008) in IC5063. Specifically, the visual extinction produced by the torus along our LOS can be computed as (see section 4.3.1 in Ramos Almeida et al. 2009):

$$A_v^{LOS} = 1.086 N_0 \tau_v e^{-((i-90)^2/\sigma^2)} \quad (2)$$

where  $N_0$  is the number of clouds along the equatorial direction;  $\tau_v$  is the optical depth of the individual clouds;  $i$  is the viewing angle; and  $\sigma$  is the torus angular width.

The most complete fit to IC5063 found in the literature, taking into account both photometry and spectroscopic data from NIR to MIR and a foreground dust screen geometry, is by Alonso-Herrero et al. (2011). We used the probabilistic distributions of the free parameters (Alonso-Herrero et al. 2011, see the blue distributions in their figure A5) in Equation 2, to obtain a posterior probabilistic distribution of the visual extinction in our LOS (for further details see Asensio Ramos & Ramos Almeida 2009; Ramos Almeida et al. 2009). Then, the median and  $\pm 1\sigma$  from the median were estimated to be  $A_v^{LOS} = 1800^{+200}_{-270}$  mag. Note that a flatter probabilistic distribution of the free parameters in the visual extinction in our LOS,  $A_v^{LOS}$ , means that a larger error is estimated.

(5) Foreground absorption. The extinction from the dust lane in the host galaxy is calculated using the (J-H) vs. (H-K<sub>n</sub>) color maps of IC5063 and its relation with visual extinction (Jones 1989). The visual extinction is measured to be  $A_v = 8 \pm 2$  mag., consistent with  $A_v = 7$  mag. obtained from dust features in the central  $1'' - 2''$  by Heisler & De Robertis (1999); and the value,  $A_v = 6 \pm 2$  mag., estimated using the polarisation model in Section 5.

A summary of the various extinction values are shown in Table 4. The extinction at different wavelengths shows that the total flux obscuration depends strongly on the wavelength and/or model used. The estimated visual extinction through the dust-to-ratio relation in (1), is due to absorption by presumably dust free clouds close to the accretion disc, the torus and absorbers in the host galaxy. Instead, the estimated visual extinction by the torus model in (4) is due to absorption of dust in all clumps along our LOS.

**Table 4.** Visual extinction at different wavelengths to the nucleus of IC5063

Method	$A_v$ [mag]
X-Ray	$131 \pm 4$
NIR polarisation	22 - 111
Polarisation Model	$54 \pm 4$
Silicate absorption	$6 \pm 1$
Foreground absorption	$8 \pm 2$
Clumpy torus model	$1800^{+200}_{-270}$

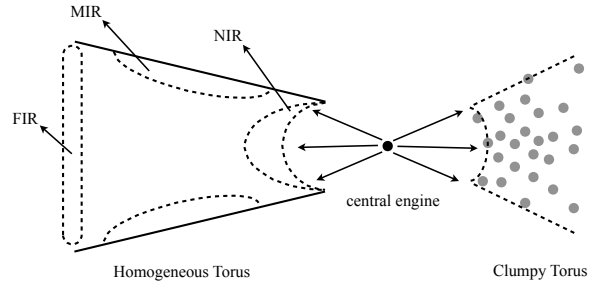


**Figure 8.** Sketch of the homogeneous (left) and clumpy torus (right). For the homogeneous torus, the inner side of the torus emits in NIR, the middle regions emit in MIR, and the outer side emits in FIR. For the clumpy torus, the NIR emission arises from the inner side of the directly illuminated clouds, while the MIR and FIR emission is produced from the shadowed side of the clumps (see Figure 9). Note that clumps located at different distances can produce the same emission at a specific wavelength. See Section 6.

Hence, the extinction calculated through these models and our polarisation model are produced by different material located in and around the torus. Based on these studies, it can be interpreted that each wavelength penetrates different depths into the obscuring torus.

The range of obscurations estimated are interpreted in terms of the dichroic absorption polarisation. Several NIR polarimetric studies (e.g., Jones & Klebe 1989; Young et al. 1995; Packham et al. 1998; Simpson et al. 2002) of AGN, have found that the nuclear polarisation of type 2 AGN typically arises through dichroic absorption within the torus to our LOS. The implications of this are (1) the total flux in the NIR wavelengths is from the directly illuminated torus inner-edge or inner-facing dust clump face (i.e. the surface of the dust clump that is directly illuminated by the central engine, Figure 8) or perhaps the central engine itself (Kishimoto et al. 2005, 2007, 2008); and (2) the NIR polarisation arises as the torus dust grains are aligned, most likely by the central engine's magnetic field (see Fig. 9).

In this scheme, an individual cloud of the clumpy torus can (dependent on the cloud's position and distribution of other clouds) absorb radiation from the central engine on the inner-facing face. This dust will re-emit radiation at NIR wavelengths in all directions. Some of this radiation will be self-absorbed by that clump, and some will be emitted into free space. A small amount of flux will be emitted and penetrate the dust clump at a glancing angle, leading

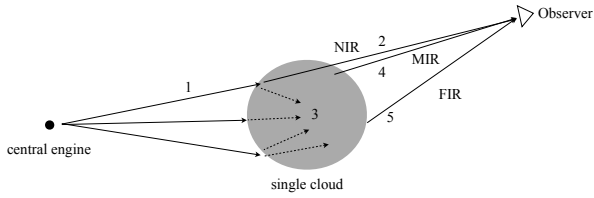


**Figure 9.** Sketch of the emission and polarisation of an individual directly illuminated cloud in the clumpy torus. (1) The central engine emits radiation that is absorbed by the cloud, (2) the radiation in the outer layers of the cloud is polarised by the passage of light through the aligned dust grains, and the NIR polarised emission can be in the direction of our LOS. (3) Those rays with direction to the nucleus of the cloud, are completely extinguished. (4) and (5) the difference of temperature in the cloud produces that the warm dust in the middle and back side of the cloud emit in MIR and FIR, respectively. See Section 6.

to obscuration and dichroic polarisation from only a portion of the dust clump (see Figure 9).

## 7 MAGNETIC FIELD STRENGTH WITHIN THE TORUS

In this section the magnetic field strength in the NIR regions of the torus of IC5063 is estimated through three different methods: (1) paramagnetic alignment; (2) magnetic relaxation time; and (3) Chandrasekhar-Fermi method. Alternatively, and as a possible component of the magnetic field strength of the torus, the magnetic field strength at 1pc from the SMBH of IC5063 have been estimated (see Appendix A).

### 7.1 Method 1: Polarisation ratio, $P/A_v(\%)$ , vs. magnetic field strength

We attributed the NIR polarisation to dichroic absorption from aligned dust grains in the clumps of the torus. The alignment can be produced by the rotational dynamics of the grain with the environment temperature and/or by the local magnetic field (Davis & Greenstein 1951). The orientation of dust grains by a magnetic field is called paramagnetic alignment, through which grains are become oriented with their long axis perpendicular to the magnetic field lines.

As a first step to considering the magnetic field responsible for the aligning the dust within the torus, we consider the physical conditions and environment of the gas and dust within the torus. The gas temperature reaches a value of  $\sim 10^4$  K in the BLR (Netzer 1987). NIR reverberation mapping of several AGN have shown that the outer radius of the BLR approximately corresponds to the inner radius of the dusty torus (Suganuma et al. 2006). Krolik & Kriss (2001) suggested that a warm absorber gas in the inner edge of the torus can reach temperatures in the range of  $10^4 - 10^6$  K. Recent 3D simulations of the interstellar medium surrounding the central engine showed that atomic gas and ionized [CII] trace well the inner regions of the torus, with temperatures in the range of  $10^4 - 10^5$  K (Pérez-Beaupuits et al. 2011). Based on these previous studies, we adopt a lower

**Table 5.** Physical parameters assumed to the calculation of the magnetic field strength in the torus of IC5063

Description	Parameter	Value
Gas temperature	$T_{\text{gas}}$	$10^4$ K
Grain temperature	$T_{\text{gr}}$	800 - 1500 K
Grain size	$a$	$10^{-6} - 10^{-5}$ cm
Column density in the cloud	$n$	$10^4 - 10^5$ cm $^{-3}$

limit in the gas temperature to be  $T_{\text{gas}} \sim 10^4$  K, in order to obtain a lower limit in the estimation of the magnetic field strength through methods (1) and (2). The NIR regions are located in the directly illuminated clumps in the torus from central engine<sup>3</sup>. Nenkova et al. (2008) estimated the dust temperatures to be in the range of 800 - 1500 K, for the directly illuminated faces of the clumps in the clumpy torus, hence we constraint the dust temperature within that range in the NIR regions studied in this paper. The temperature range is dependent on the size and grain type i.e. graphite and/or astronomical-silicates (Nenkova et al. 2008). Based on the range of temperatures, the grain size is assumed to be in the range of 0.001 - 0.01  $\mu\text{m}$ . The column densities of individual clouds was calculated specifically for IC5063, assuming the following parameters: (1) Alonso-Herrero et al. (2011) obtained a radius of 2.4 pc and a number of clouds along the equatorial direction of  $14 \pm 1$  from the clumpy torus model; and (2) the gas column densities, as derived from NIR molecular hydrogen lines, ranging  $1 - 10 \times 10^{23}$  cm $^{-2}$  (Davies et al. 2006; Hicks et al. 2009). The column density for individual clouds in the torus of IC5063 is in the range of  $10^4 - 10^5$  cm $^{-3}$ . A summary of these physical parameters is shown in Table 5.

Models of paramagnetic alignment have been highly successfully applied to studies of dust grains in molecular clouds (i.e. Lazarian 1995; Gerakines et al. 1995). These studies correlate the polarisation,  $P(\%)$ , with dust extinction,  $A_v$ , as a function of the magnetic field strength,  $B$ , modeled by Vrba, Cyne, & Tapia (1981). The efficiency of dust grains, defined as  $P(\%)/A_v$ , is directly proportional with the average alignment of the grains, and depends of the physical conditions of the environment as well as the magnetic field strength,  $B$ . An adapted version from equation 8 in their paper is presented here to be:

$$P(\%)/A_v = \frac{67\chi''B^2}{75a\omega n} \left( \frac{2\pi}{m_H k T_{\text{gas}}} \right)^{1/2} (\gamma-1) \left( 1 - \frac{T_{\text{gr}}}{T_{\text{gas}}} \right) \quad (3)$$

where,  $\chi''$ , is the imaginary part of the complex electric susceptibility, a measure of the attenuation of the wave caused by both absorption and scattering;  $B$  is the magnetic field strength;  $\gamma$  is the ratio of inertia momentum of the dust grains;  $T_{\text{gr}}$ , is the grain temperature;  $a$ , is the grain size;  $\omega$ , is the orbital frequency of the grains;  $n$ , is the column density in the cloud;  $m_H$ , is the mass of a hydrogen atom;  $k$ , is the Boltzmann constant; and  $T_{\text{gas}}$ , is the gas temperature.

Purcell (1969) showed that the lower bound for the most

<sup>3</sup> Note that several authors (Mor et al. 2009; Mor & Netzer 2012) argued that the NIR emission can not be related with dust within the torus, but located in inner regions than the inner edge of the torus.

interstellar grains, the ratio  $\chi''/\omega$  is (see review Aannestad & Purcell 1973)

$$\frac{\chi''}{\omega} = 2 \times 10^{-12} T_{\text{gr}}^{-1} \quad (4)$$

The ratio of the moment of inertia of the dust grains,  $\gamma$ , is defined as:

$$\gamma = \frac{1}{2} \left[ \left( \frac{b}{a} \right)^2 + 1 \right] \quad (5)$$

where  $\frac{b}{a}$  is the grain axial ratio. A typical value of  $b/a$  for interstellar dust grains is  $\sim 0.2$  (Aannestad & Purcell 1973; Kim & Martin 1995).

Equation (3) was modeled for optical (V band) wavelengths by Vrba, Cyne, & Tapia (1981). Further studies (Gerakines, Whittet, & Lazarian 1995) showed that it is also applicable at K band. Using the physical conditions in Table 5, the intrinsic polarisation arising from dichroic absorption  $P_{K_n}^{\text{dic}} = 12.5 \pm 2.7\%$  and the extinction through the torus,  $A_V(1) = 48 \pm 4$  mag, at  $K_n$ ,  $A_{K_n} = 5 \pm 2$  mag. The magnetic field strength was estimated to be in the range of 12 - 128 mG for the NIR emitting regions of the torus of IC5063.

We can compare our estimated magnetic field strength to previous published values. Polarimetric observations with the VLA and the GBT at 22GHz of the water vapor masers in NGC 4258, estimated the value of a toroidal magnetic field strength of 90 mG at 0.2 pc (Modjaz et al. 2005). Circular polarisation observations of NGC4258 estimated an upper-limit of the magnetic field strength in the maser features to be 300 mG (Herrnstein et al. 1998). Kartje et al. (1999) estimated an lower-limit of the magnetic field strength in the maser clouds of AGN to be 20 mG. These studies considered outflow winds confined in magnetic field lines generated in the central engine. Although for different objects, and at different spatial locations, our derived range of magnetic field strength compares well with these previous studies.

To estimate the magnetic field strength in the torus of IC5063, several assumptions were made. Here, we consider each of these assumptions in detail. The dust grains of the torus clumps almost certainly experience much more turbulent and extreme physical conditions than molecular clouds (Vrba et al. 1981; Lazarian 1995; Gerakines et al. 1995), which in molecular clouds makes the alignment of dust grains less responsive to the magnetic field.

We assumed a homogeneous magnetic field, where any inhomogeneities in the torus are ignored. This assumption has some implications for the ratio,  $P(\%)/A_V$ . If a homogeneous magnetic field is responsible for dust grain alignment in the torus clumps, then all the dust grains will be aligned along the same orientation of the magnetic field line. In this case, the ratio  $P(\%)/A_V$  will maximize the alignment efficiency, and hence the degree of polarisation would decrease when inhomogeneities of the magnetic field are present. We interpret the magnetic field strength from Method 1, as a lower-limit to the magnetic field.

The method used here shows a strong dependence of grain sizes. Based on our interpretation of the extinction and polarising modeling, the grain sizes can be constrained. The physical conditions in the inner side of the torus (i.e. high temperature and direct radiation from the central engine) makes impossible any evolutionary grown of the grains in

such region. Hence, only small grain can survive (0.001-0.1  $\mu\text{m}$ ). Although this physical condition allows us to refine the grains sizes ranges, the effect of the grain sizes in the above methods are difficult to quantify.

Thus, our estimate of the magnetic field strength in the range of 12 - 128 mG represents a lower-limit for the NIR emitting regions of the torus of IC5063.

## 7.2 Method 2: Magnetic relaxation time

Roberge, DeGraft, & Flaherty (1993) developed a computational method to solve the grain alignment problem in molecular clouds. They found that the approach followed in Method 1 (Section 7.1) is valid only when the ratio of thermal to magnetic relaxation time is smaller than unity. In order to verify this condition, we calculate the lower-limit magnetic field strength required to satisfy this condition.

In the previous section, we assumed that the dust grains in the torus clumps are uniquely aligned by the presence of a magnetic field. This assumption is valid if the magnetic field is strong enough to dominate over both the turbulence within the torus clump and the rotational dynamics of the clump environment. For rotational dynamic mechanism, the dust grains are aligned when the rotational kinetic energy is coupled to the grain rotation in equilibrium with the gas temperature. The time for the dust grains to be aligned by this mechanism is given by the thermal relaxation time (Hildebrand 1988),

$$t_{\text{thermal}} = \frac{2a\rho}{3n_{\text{mH}}} \left( \frac{\pi m_{\text{H}}}{8kT_{\text{gas}}} \right)^{1/2} \quad (6)$$

where,  $\rho$ , is the grain density.

In the case of magnetic alignment, the time for the grains to be aligned, is given by the magnetic relaxation time (Hildebrand 1988),

$$t_{\text{mag}} = 1.6 \times 10^{11} \frac{a^2 \rho T_{\text{gr}}}{B^2} \quad (7)$$

Assuming paramagnetic alignment in the clouds of the clumpy torus, then the magnetic field is strong enough to align the dust faster than the rotational kinetic energy. In other words, the magnetic relaxation time is required to be shorter than the thermal relaxation time. i.e.  $t_{\text{thermal}} > t_{\text{mag}}$ . Using Equations (6) and (7), a lower-limit of the magnetic field strength verifying that condition can be estimated:

$$B^2 > 2.4 \times 10^{11} a n_{\text{mH}} T_{\text{gr}} \left( \frac{8kT_{\text{gas}}}{\pi m_{\text{H}}} \right)^{1/2} \quad (8)$$

The magnetic field strength is  $> 2$  mG and  $> 30$  mG, for the physical conditions shown in Table 5. Note, these values are purely theoretical and assume stable physical conditions in the clouds of the clumpy torus. Hence, these values are considered as a lower-limit magnetic field strength in the clumpy torus of IC5063. Since the estimated magnetic field strength in Section 7.1 are larger than the lower-limit calculated here, the condition by Roberge, DeGraft, & Flaherty (1993) is satisfied in Method 1.

Under the condition that the magnetic relaxation time is shorter than the thermal relaxation time, the gas and dust temperatures are decoupled. This assumption has two

implications (1) is only valid in low-density regions in clouds; and (2) the ratio  $P(\%)/A_v$  is dependent of the magnetic field strength. In our scheme described in Section 6, the detected radiation passed through the low-density regions of the torus clump, satisfying the condition described above, applied in this section. Also, the allowance in the estimation of the magnetic field strength in Method 1.

### 7.3 Method 3: Chandrasekar-Fermi method

The Chandrasekhar-Fermi method (Chandrasekhar & Fermi 1953) was also used to estimate the magnetic field strength in the torus of IC5063. This method relates the magnetic field strength with the dispersion in polarisation angles of the constant component of the magnetic field and the projection of the mean magnetic field on the plane of the sky (hereafter termed dispersion of polarisation angles,  $\alpha$ ) and the velocity dispersion of the dust. Here (Equation 9), we use the equation 8 of Marchwinski, Pavel, & Clemens (2012). This relationship is an adapted version of equation 7 in Chandrasekhar & Fermi (1953) with the factor 0.5 introduced by Ostriker, Stone, & Gammie (2001) to estimate the magnetic field strength in the plane of the sky.

$$B = 0.5 \left( \frac{4}{3} \pi \rho \right)^{1/2} \frac{\sigma_v}{\alpha} \quad [\mu\text{G}] \quad (9)$$

where  $\rho$  is the volume mass density in  $\text{g cm}^{-3}$ ;  $\sigma_v$  is the velocity dispersion in  $\text{cm s}^{-1}$ ; and  $\alpha$  is the dispersion of polarisation angles in radians.

The volume mass density was calculated using the column mass density in Table 5 multiplied by the weight of molecular hydrogen. The velocity dispersion in masers observations in NGC 3079 is estimated to be  $14 \text{ km s}^{-1}$  at a distance of  $\sim \text{pc}$  from the central engine (Kondratko et al. 2005). Based on the magnetohydrodynamical wind model for the torus in AGN, Elitzur & Shlosman (2006) assumed velocity dispersion in the order of  $10 \text{ km s}^{-1}$ . Based on these previously published results, we use a velocity dispersion of  $10 \text{ km s}^{-1}$ . We note that the assumed value of the velocity dispersion represent a lower-limit. In order to calculate the dispersion of polarisation angles,  $\alpha$ , we used the model by Jones, Klebe, & Dickey (1992, hereafter JKD). This model relates the degree of polarisation at K with the level of turbulence in the interstellar medium and the magnetic field. In the case of IC5063, using the intrinsic polarisation arising from dichroic absorption,  $P_{K_n}^{\text{dic}} = 12.5 \pm 2.7\%$ , and the extinction by the torus,  $A_v(1) = 48 \pm 2 \text{ mag}$ , we found that our data in the JKD model (Figure 10) is located between (1) the constant component in the magnetic field; and (2) the equal contribution of the constant and random components. If we assume that the constant component of the magnetic field is in the plane of the sky, the dispersion of polarisation angles is estimated to be  $\alpha = 4.5^\circ$  ( $0.0785 \text{ radians}$ ) for our data point in Figure 10. In Equation 9 we substituted the above numerical values and we estimated a lower-limit of the magnetic field strength in the plane of the sky to be 13 and 41 mG depending of the conditions within the torus of IC5063.

We assumed that the constant component of the magnetic field strength is in the plane of the sky. If the constant component of the magnetic field is angled away from the plane of the sky, then the magnetic field strength found here

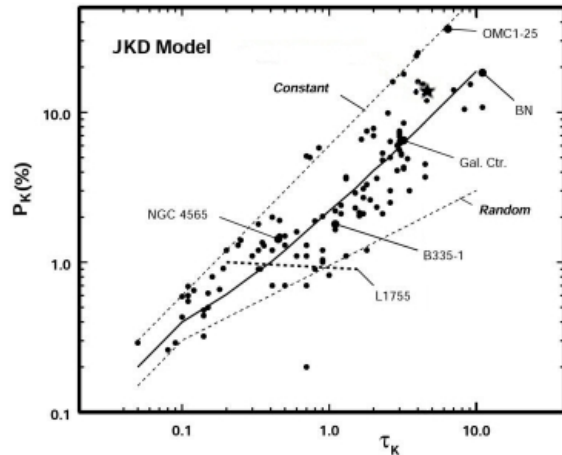


**Figure 10.** K band degree of polarisation versus optical depth. Data from Jones (1989) (black points) with some of labeled object are shown. JKD model assuming constant,  $P_K = \tanh \tau_K$ , (top dashed line) and random,  $P_K \propto \tau_K^{1/2}$ , (bottom dashed line) components; and equal contributions from both constant and random components,  $P_K = 2.23 \tau_K^{3/4}$ , (solid line) are shown. Our data,  $P_{K_n}^{\text{dic}} = 12.5 \pm 2.7\%$  and  $A_v(1) = 48 \pm 2 \text{ mag}$ , is shown (star). See Section 7.3.

**Table 6.** Magnetic field strength from three different methods

Method	$B_{\text{min}}$ (mG)	$B_{\text{max}}$ (mG)
1: Polarisation ratio vs. magnetic field strength	12	128
2: Magnetic relaxation time	2	30
3: Chandrasekhar-Fermi method	13	41
4: Magnetic field from central engine at 1pc	5	53

**Note:** All values represent a lower-limit of the magnetic field.

will be an underestimate, for example if the magnetic field line is pointed to our LOS, we will measure zero polarisation.

A summary of the estimated magnetic field strength through the four methods are shown in Table 6.

## 8 CONCLUSIONS

We presented NIR polarisation at J, H and  $K_n$  of the nuclear regions of IC5063. The analysis shows a highly polarised source, measured to be  $7.8 \pm 0.5\%$  at  $K_n$ , with a wavelength-independent PA of polarisation of  $3 \pm 6^\circ$  in the three filters. For the first time in polarised light of IC5063, the biconical ionisation cones are observed, showing a spatial correspondence with the [OIII] ionisation cones and the radio structure at 8GHz, entirely consistent with unified models.

We developed a polarimetric model to account for the various mechanisms of polarisation in the central  $1.2''$  ( $\sim 263 \text{ pc}$ ) aperture of IC5063. To account for the scattering pattern produced by the biconical structure observed at H, an additional polarising component due to electron scattering was required. The model of the nuclear polarisation at  $K_n$  is consistent with the polarisation being produced through dichroic absorption from aligned dust grains in the

clumps of the torus with a visual extinction  $A_v = 48 \pm 2$  mag. by the torus.

Through the use of various components to the central engine of IC5063, we estimated the intrinsic polarisation arising from dichroic absorption to be  $P_{K_n}^{\text{dic}} = 12.5 \pm 2.7\%$  at  $K_n$  in a  $1.2''$  aperture. Estimates of the extinction to the central engine of IC5063 at X-ray, NIR and MIR showed a wide variations in the extinction depending on the wavelengths on which the estimated is based on. We interpreted as that different wavelengths resulting from different emission locations within the torus and hence suffering different level of obscuration. In this scheme, an individual cloud of the clumpy torus can, depending on the cloud position and distribution of other cloud, absorb radiation from the central engine on the inner-facing face. This dust will re-emit radiation at NIR wavelengths in all directions. Some of this radiation will be self-absorbed by that clump, and some will be emitted into free space. A small amount of flux will be emitted and penetrate the dust clump at a glancing angle, leading to obscuration and dichroic polarisation from only a portion of the dust clump.

We assumed the alignment of dust grains be produced by paramagnetic relaxation. Then, the intrinsic polarisation and visual extinction ratio,  $P(\%)/A_v$ , is a function of the magnetic field strength. We considered the physical conditions and environments of the gas and dust within the torus and we estimated the magnetic field strength in the range of 12 - 128 mG for the NIR emitting regions of the torus of IC5063. Alternatively, we estimate the magnetic field strength in the plane-of-sky using the Chandrasekhar-Fermi method. The minimum magnetic field strength in the plane-of-sky is estimated to be 13 and 41 mG depending of the conditions within the torus of IC5063.

These studies, to our knowledge, provide the first approach investigating the magnetic field of the torus in AGN through NIR polarisation. Further NIR polarimetric observations of IC5063 and other AGN are required to refine and/or modify this approach. The next generation of polarimeters, such as adaptive optics optimized imaging polarimeter in the NIR (1-5  $\mu\text{m}$ ) MMT-POL (Packham & Jones 2010) at the 6.5m MMT, the MIR polarimeter (7.5-13  $\mu\text{m}$ ) CanariCam (Packham et al. 2005) at the 10.4-m GTC will provide a high spatial resolution and polarisation sensitivity that will allow us to refine and/or modify these studies. Also, mm-polarimetric observations with ALMA will allow to refine intrinsic properties of the torus, i.e. dust density, grain sizes, temperature, used in the methodology to calculate the magnetic fields.

## ACKNOWLEDGMENTS

E. Lopez-Rodriguez acknowledges support from an University of Florida Alumni Fellowship and C. Packham from NSF-0904421 grant. C. Ramos Almeida acknowledges financial support from the Spanish Ministry of Science and Innovation (MICINN) through project Consolider-Ingenio 2010 Program grant CSD2006-00070: First Science with the GTC<sup>4</sup> and the Estallidos group through project PN

AYA2010-21887-C04.04. A. Alonso-Herrero acknowledges support from the Spanish Plan Nacional de Astronomía y Astrofísica under grant AYA2009-05705-E. Supported by the Gemini Observatory, which is operated by the Association of Universities for Research in Astronomy, Inc., on behalf of the international Gemini partnership of Argentina, Australia, Brazil, Canada, Chile, the United Kingdom, and the United States of America. E. Perlman acknowledges financial support from NSF under grant NSF-09040896. We also thank an anonymous referee for a number of helpful comments.

## REFERENCES

- Aannestad, Purcell, 1973, ARA&A, 11, 309
- Alonso-Herrero A. et al., 2011, ApJ, 736, 82
- Angel J. P. R. et al., 1978, bllo.conf, 117
- Antonucci R., 1993, ARA&A, 31, 473
- Antonucci R. R. J., Miller J. S., 1985, ApJ, 297, 621
- Asensio Ramos A., Ramos Almeida C., 2009, ApJ, 696, 2075
- Axon D. J., Bailey J. A., Hough J. H., 1982, Nature, 299, 234
- Bailey J., Hough J. H., Axon D. J., 1983, MNRAS, 203, 339
- Bergeron J., Durret F., Bokserberg A., 1983, A&A, 127, 322
- Blandford R. D., Payne D. G., 1982, MNRAS, 199, 883
- Bohlin R. C., Savage B. D., Drake J. F., 1978, ApJ, 224, 132
- Boisson C., Durret F., 1986, A&A, 168, 32
- Brindle C., Hough J. H., Bailey J. A., Axon D. J., Sparks W. B., 1990, MNRAS, 247, 327
- Campins H., Rieke G. H., Lebofsky M. J., 1985, AJ, 90, 896
- Chandrasekhar S., Fermi E., 1953, ApJ, 118, 113
- Colina L., Sparks W. B., Macchetto F., 1991, ApJ, 370, 102
- Davies R. I. et al., 2006, ApJ, 646, 754
- Davis L. J., Greenstein J. L., 1951, ApJ, 114, 206
- de Vaucouleurs G., de Vaucouleurs A., Corwin H. G. J., Buta R. J., Paturel G., Fouqué P., 1991, Third Reference Catalogue of Bright Galaxies, V3.9
- Elitzur M., Shlosman I., 2006, ApJ, 648, L101
- Emmering R. T., Blandford R. D., Shlosman I., 1992, ApJ, 385, 460
- Evans I. N., Ford H. C., Kinney A. L., Antonucci R. R. J., Armus L., Caganoff S., 1991, ApJ, 369, L27
- Gerakines P. A., Whittet D. C. B., Lazarian A., 1995, ApJ, 455, 171
- Gillingham P. P., Lankshear A. F., 1990, Proc. SPIE, 1235, 9
- Greenberg J. M., 1978, John Wiley & Sons, 187
- Heisler C. A., De Robertis M. M., 1999, ApJ, 118, 2038
- Herrnstein J. R., Moran J. M., Greenhill L. J., Blackman E. G., Diamond P., 1998, ApJ, 508, 243
- Hicks E. K. S., Davies R. I., Malkam M. A., Genzel R., Tacconi L. J., Muller Sanchez F., Sternberg A., 2009, ApJ, 696, 448
- Hildebrand R. H., 1988, ApL&C, 26, 263

<sup>4</sup> <http://www.iac.es/consolider-ingenio-gtc/>

- Hough J. H., Brindle C., Axon D. J., Bailey J. A., Sparks W. B., 1987, *MNRAS*, 224, 1013
- Hough J. H., Chrysostomou A., Bailey J. A., 1994, *Experimental Astronomy*, 3, 127
- Hunt L. K., Massi M., Zhekov S., 1994, *A&A*, 290, 428
- Impey C. D., Neugebauer M., 1988, *AJ*, 95, 307
- Inglis M. D., Brindle C., Hough J. H., Young S., Axon D. J., Bailey J. A., Ward M. J., 1993, *MNRAS*, 263, 895
- Jaffe W. et al., 2004, *Nature*, 429, 47
- Jones T. J., 1989, *ApJ*, 346, 728
- Jones T. J., Klebe D., 1989, *ApJ*, 341, 707
- Jones T. J., Klebe D., Dickey J. M., 1992, *ApJ*, 389, 602
- Kartje J. F., Konigl A., Elitzur M., 1999, *ApJ*, 513, 180
- Kim J., Martin P. G., 1995, *ApJ*, 444, 293
- Kishimoto M., Antonucci R. R. J., Blaes O., 2005, *MNRAS*, 364, 640
- Kishimoto M., Antonucci R. R. J., Blaes O., Lawrence A., Boisson C., M. A., Leipski C., 2008, *Nature*, 454, 492
- Kishimoto M., Honig S. F., Beckert T., Weigelt G., 2007, *A&A*, 476, 713
- Kondratko P. T., Paul T., Greenhill L. J., Moran J. M., 2005, *ApJ*, 618, 618
- Krolik J. H., Begelman M., 1988, *ApJ*, 329, 701
- Krolik J. H., Kriss G. A., 2001, *ApJ*, 561, 684
- Kulkarni V. P. et al., 1998, *ApJ*, 492, L121
- Landini M., Natta A., Salinari P., Oliva E., Moorwood A. F. M., 1984, *A&A*, 134, 284
- Lazarian A., 1995, *ApJ*, 453, 229
- Lazarian A., 2007, *JQSRT*, 106, 205
- Levenson N., Radomski J. T., Packham C., Mason R. E., Schaefer J. J., Telesco C. M., 2009, *ApJ*, 703
- Marchwinski R. C., Pavel M. D., Clemens D. P., 2012, *ApJ*, 755, 130
- Martin P. G., Whittet D. C. B., 1990, *ApJ*, 357, 113
- Mason R., Geballe T. R., Packham C., Levenson N., Elitzur M., Fisher S., Perlman E., 2006, *ApJ*, 640, 622
- Mason R., Wright G., Adamson A., Pendleton Y., 2007, *ApJ*, 656, 797
- Modjaz M., Moran J. M., Kondratko P. T., Greenhill L. J., 2005, *ApJ*, 626, 104
- Mor R., Netzer H., 2012, *MNRAS*, 420, 526
- Mor R., Netzer H., Elitzur M., 2009, *ApJ*, 705, 298
- Morganti R., Holt J., Saripalli L., Oosterloo T. A., Tadhunter C. N., 2007, *A&A*, 476, 735
- Morganti R., Oosterloo T., Tsvetanov Z., 1998, *AJ*, 115, 915
- Nagata T., 1990, *ApJ*, 348, 13
- Nenkova M., Izevic Z., Elitzur M., 2002, *ApJ*, 570, L9
- Nenkova M., Sirocky M. M., Izevic Z., Elitzur M., 2008, *ApJ*, 685, 147
- Netzer H., 1987, *MNRAS*, 225, 55
- Neugebauer M., Soifer B., Matthews K., Elias J. H., 1989, *AJ*, 97, 957
- Ostriker E. C., Stone J. M., Gammie C. F., 2001, *ApJ*, 546, 980
- Packham C., Hough J. H., Young S., Chrysostomou A., Bailey J. A., Axon D. J., Ward M. J., 1996, *MNRAS*, 278, 406
- Packham C., Jones T. J., 2010, *SPIE*
- Packham C., Radomski J. T., Roche P. F., Aitken D. K., Perlman, E. and Alonso-Herrero A., Colina L., Telesco C., 2005, *ApJ*, 618, L17
- Packham C. et al., 2007, *ApJ*, 661, L29
- Packham C., Young S., Hough J. H., Axon D. J., Bailey J. A., 1997, *MNRAS*, 288, 375
- Packham C., Young S., Hough J. H., Tadhunter C. N., Axon D. J., 1998, *MNRAS*, 297, 936
- Pariev V. I., Blackman E. G., Boldyrev S. A., 2003, *A&A*, 407, 403
- Pérez-Beaupuits J. P., Wada K., Spaans M., 2011, *ApJ*
- Purcell, 1969, *ApJ*, 158, 433
- Radomski J. T., Pina R. K., Packham C., Telesco C. M., De Buizer J. M., Fisher R. S., Robinson A., 2003, *ApJ*, 587, 117
- Radomski J. T., Pina R. K., Packham C., Telesco C. M., Tadhunter C. N., 2002, *ApJ*, 566, 675
- Ramos Almeida C. et al., 2011, *ApJ*, 731, 92
- Ramos Almeida C. et al., 2009, *ApJ*, 702, 1127
- Roberge W., DeGraff T. A., Flaherty J. E., 1993, *ApJ*, 418, 287
- Schartmann M., Krause M., Burkert, 2011, *MNRAS*, 415, 741
- Schmitt H. R., Donley J. L., Antonucci R. R. J., Hutchings J. B., Kinney A. L., 2003, *ApJS*, 148, 327
- Serkowski K., Mathewson D. S., Ford V. L., 1975, *ApJ*, 196, 261
- Silant'ev N. A., Gnedin Y. N., Buliga S. D., Piotrovich M. Y., Natsclishcili T. M., 2012, *arXiv*, 1203.2763
- Silant'ev N. A., Piotrovich M. Y., Gnedin Y. N., Natsvlshvili T. M., 2009, *A&A*, 507, 171
- Simpson C., Ward M., Kotilainen J., 1994, *MNRAS*, 271, 250
- Simpson J. P., Colgan S. J., Erickson E. F., Hines D. C., Schultz A. S. B., Trammell S. R., 2002, *ApJ*, 574, 95
- Sparks W. B., Hough J. H., Axon D. J., Bailey J., 1986, *MNRAS*, 218, 429
- Suganuma M. et al., 2006, *ApJ*, 636, 639
- Tadhunter C. N. et al., 2000, *MNRAS*, 313, 52
- Tazaki F., Ueda Y., Terashima Y., Mushotzky R. F., 2011, *ApJ*, 738, 70
- Tinbergen J., 1996, *Astronomical Polarimetry*. Cambridge University Press
- Tristram K. R. W. et al., 2007, *A&A*, 474, 837
- Turner P. C., Forrest W. J., Pipher J. L., Shure M. A., 1992, *ApJ*, 393, 648
- Urry C. M., Padovani P., 1995, *PASP*, 107, 803
- Vasudevan R. V., Fabian A. C., Gandhi P., Winter L. M., Mushotzky R. F., 2010, *MNRAS*, 402, 108
- Vrba, Cyne, Tapia, 1981, *ApJ*, 243, 489
- Wada K., Papadopoulos P. P., Spaans M., 2009, *ApJ*, 702, 63
- Whittet D. C. B., 1987, *QJRAS*, 28, 303
- Whittet D. C. B., Gerakines P. A., Hough J. H., Shenoy S. S., 2001, *ApJ*, 547, 872
- Whittet D. C. B., Martin P. G., Hough J. H., Rouse M. F., Bailey J. A., Axon D. J., 1992, *ApJ*, 386, 562
- Young S., Hough J. H., Axon D. J., Bailey J. A., Ward M. J., 1995, *MNRAS*, 272, 513
- Young S., Packham C., Mason R., Radomski J. T., Telesco C., 2007, *MNRAS*, 378, 888

**APPENDIX A: MAGNETIC FIELD FROM THE CENTRAL ENGINE**

The central engine generates a magnetic field. The magnetic field at a given distance is proportional to the (a) magnetic field of the super massive black hole (SMBH); and (b) distance from the SMBH, following a power-law function, given by  $B = B_{\text{BH}} \left( \frac{r}{r_{\text{BH}}} \right)^{-n}$  (e.g., Silant'ev et al. 2009). The magnetic field strength at the horizon event is  $B_{\text{BH}}$ , and  $r_{\text{BH}}$ , is the radius of the black hole horizon, which is dependent of the black hole mass,  $M_{\text{BH}}$ . The power-law index,  $n$ , is taken as  $5/4$  from the assumed optical thin magnetically dominated accretion disc from  $5r_{\text{BH}} < r < 100r_{\text{BH}}$  most physically significant model of Pariev et al. (2003); and further used by Silant'ev et al. (2009). In the case of IC5063, the black hole mass,  $M_{\text{BH}} = 2.6 \times 10^7 M_{\odot}$  was estimated by Vasudevan et al. (2010), using the mass-luminosity relation and Two-Micron All-Sky Survey (2MASS) image at K-band. For black hole masses of  $\sim 10^7 M_{\odot}$ , Silant'ev et al. (2012) estimated magnetic field strength at the event horizon in the range of  $B_{\text{BH}} = 10^4 - 10^5$  G. Using these values in the above power-law function, the range of magnetic field strength is 5 - 53 mG at 1pc from the horizon event of the SMBH of IC5063.

This paper has been typeset from a  $\text{\LaTeX}$  file prepared by the author.